Quantum Electronics **52** (6) 587–592 (2022)

INTERACTION OF LASER RADIATION WITH MATTER https://doi.org/10.1070/QEL18068

Specificity of micro- and nanoproducts of titanium laser ablation in pure water

T.I. Borodina, G.E. Val'yano, M.M. Malikov

Abstract. **Laser ablation of titanium in distilled water at high and low power densities of copper vapour laser beam in the focal spot on a target surface is experimentally studied. Ablation regimes with different pulsed energy inputs and target irradiation times are investigated. The morphology and elemental and phase compositions of micro- and nanoaggregates obtained in different irradiation regimes are studied using electron microscopy, X-ray diffraction analysis, and Raman spectroscopy. The ablation products are found to be practically totally in the X-ray amorphous state.**

Keywords: *titanium, laser ablation in water, nanostructures, oxides, amorphous products.*

1. Introduction

Laser ablation of metal targets placed in a liquid is a relatively simple and convenient way to form (in small amounts) various nanoparticles of target metals, their oxides, and other compounds, both in crystalline and amorphous states [1, 2]. When a target surface is exposed to a high-power laser pulse, a plasma/vapour plume is ejected into the surrounding liquid, and a bubble arises, within which the temperature and pressure reach large values. Upon subsequent cooling and destruction of bubbles, a colloidal solution of individual nanoparticles and their agglomerates is formed. In addition, the newly formed particles drift in the liquid to enter again the focused-beam region and be subjected again to the multiple effect of laser pulses, which may change their properties and sizes. Diverse mechanisms of the formation and evolution of nano- and microstructures were discussed, e. g., in [3–6]. All these processes and the final ablation product depend in many respects on the laser beam parameters on the target surface, such as the wavelength λ, densities of power P_{las} and energy E_{las}, pulse duration τ_p, pulse repetition rate f, and target irradiation time τ_{irr}. Note that the final product is also affected by the liquid composition and aging time of the obtained colloid of nanoparticles. Therefore, it is important to perform corresponding experiments using different lasers under different conditions and compare the results obtained.

In this work we used a copper vapour laser (CVL) to perform titanium ablation in distilled water. Experiments were carried out in two target irradiation regimes with significantly different laser beam parameters in order to study their influence on the titanium ablation in water. Similar experiments under conditions close to those used by us were performed in [4, 7, 8]; hence, one can compare the results and draw certain conclusions about the role of particular factors affecting the composition and morphology of dried colloidal precipitates. Note that the analysis of the properties of nanoparticles of various titanium oxides is of great interest from the point of view of different practical applications [9–11], for example, their use as substrates in the technique of surface-enhanced Raman scattering (SERS) in diagnostics of gas-dynamic fluxes and plumes [12, 13].

T.I. Borodina, G.E. Val'yano, M.M. Malikov Joint Institute for High Temperatures, Russian Academy of Sciences, ul. Izhorskaya 13, stroenie 2, Moscow, 125412 Russia; e-mail: mmalikov@oivtran.ru

Received 22 December 2021; revision received 12 April 2022
Kvantovaya Elektronika **52** (6) 587–592 (2022)
Translated by Yu.P. Sin'kov

2. Description of the experiment, ablation conditions, and techniques of nanostructure analysis

The experiments on laser ablation of VT1-0 (99%) titanium in distilled water were performed using the system described in [14]. The radiation source was a repetitively pulsed CVL ($\lambda = 0.51$ and 0.578 μm, $\tau_p \approx 20$ ns, $f = 10$ kHz). In the first regime the average laser power was $W \approx 10–13$ W, the pulse energy was $E_p \approx 1.0–1.3$ mJ, and the peak power was ~50–65 kW. Application of an achromatic lens with a focal length of 190 mm provided a spot ~50 μm in diameter on the target surface. The energy density and laser beam power in the spot were, respectively, 50–65 J cm^{-2} and $(2.5–3.2) \times 10^9$ W cm^{-2}. In the second regime the average and peak laser powers were reduced by an order of magnitude (~1 W and ~5 kW, respectively) using a plane-parallel glass plate (BS-3), which reflected about 10% radiation at an angle of ~45° towards the focusing lens. The diameter of the beam reflected by the plate (20 mm) and the power density distribution in its cross section remained the same, because the plane-parallel plate did not introduce any significant distortions. In this regime the laser energy and power densities in the focus were, respectively, ~5 J cm^{-2} and $\sim 2.5 \times 10^8$ W cm^{-2}.

A titanium target ~5 mm thick and 16 mm in diameter was placed on the bottom of a cell filled with distilled water (4.5 mL), which rotated with a speed of ~2 rpm, so that the irradiation spot moved over the target surface. The target irradiation time τ_{irr} was ~30–50 min in these experiments.

The colloidal solution obtained as a result of ablation was deposited on special substrates and dried at 50 °C – 70 °C. Preliminary centrifugation of the colloid (with a speed of 10^4 rpm for 30 min) and subsequent drying of the precipitate were performed in some experiments.

The morphology of microstructures and elemental composition of the dried preparations were investigated using a

scanning electron microscope (SEM) Nova NanoSem 650, equipped with an EDS system for recording and analysing characteristic X-ray (CXR) spectra. The preparations were deposited on copper substrates. Note that the EDS data yield an estimate of the elemental content averaged over the volume of CXR generation region (~1.5 μm in diameter). In addition, an annular backscattered electron detector was used, which makes it possible to increase the contrast in SEM images of microstructural elements.

The phase compositions of the products were investigated using X-ray diffraction (XRD) and Raman spectrometry. XRD spectra were recorded on DRON-2 and SmartLab (Rigaku) diffractometers according to the standard technique. In both cases CuK_α radiation was used. The Raman spectra of the precipitates were analysed with a Raman automatic spectrograph U1000 (JOBIN-YVON). The wavelength of the initial laser beam (used to excite Raman scattering) was 514.53 nm, and the beam diameter amounted to ~20–30 μm. Note that preparations on glass and silicon plates were used for XRD analysis and Raman spectroscopy, respectively.

3. Experimental results

The appearance of the colloids, obtained in the first regime (35-min exposure to high-power laser radiation) is presented in Fig. 1. By the end of the irradiation the colloid had a bluish-gray colour and was slightly turbid. After a long time (15–20 h) a precipitate in the form of macroscopic aggregates, fairly large (~1–3 mm) in the cross section and very thin (resembling 'flakes') appeared on the cell bottom (Fig. 1a). Above the flakes the colloid was transparent. Being agitated, the colloid became turbid, and the flakes disappeared; however, 30–60 min later a precipitate arose again on the bottom, also in the form of flakes but of smaller size. After the agitation the turbid colloid was poured into a special test tube and then subjected to centrifugation. As a result, we obtained a grey blue precipitate on the bottom of the test tube (Fig. 1b), which visually differed very much from that shown in Fig. 1a.

To analyse the ablation products in the first case, we used the upper transparent layer of the colloid presented in Fig. 1a; in the second case, the object of study was a colloid carefully mixed in the cell; and, in the third case, we investigated the centrifuged precipitate on the bottom of the test tube (Fig. 1b).

The colloid obtained in the second regime of laser irradiation of a titanium target in water had a pinkish hue and was transparent, both by the end of irradiation and for the next several hours. After 10–15 h, a precipitate similar to that shown in Fig. 1a, but in smaller amounts, arose.

3.1. Structural morphology of colloidal precipitates

The micro- and nanostructural morphology of the precipitates of colloids obtained by titanium ablation in distilled water is demonstrated by SEM images.

The structure of the precipitates for the first irradiation regime is shown in Figs 2 and 3.The precipitate obtained

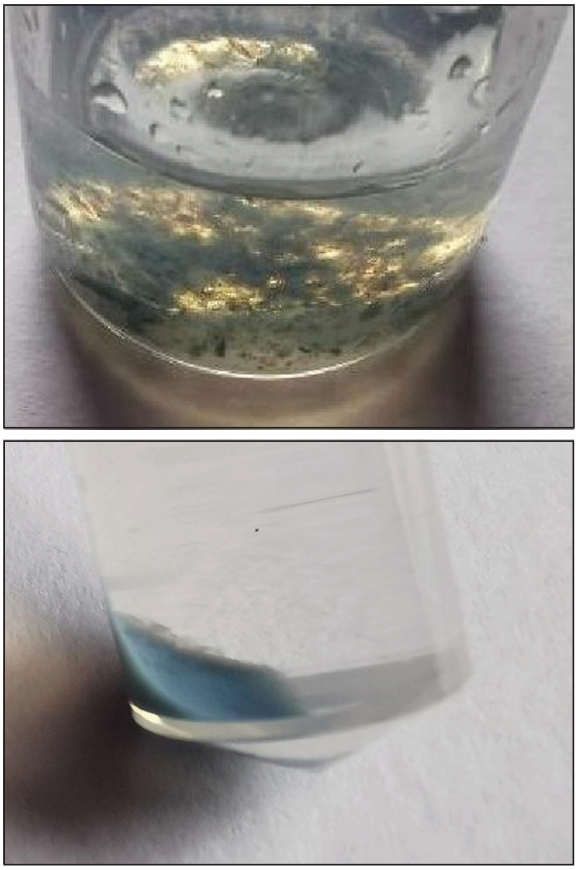

Figure 1. (Colour online) Appearance of the colloids obtained by titanium ablation in water in the first irradiation regime ($W \approx 12$ W, $\tau_{irr} \approx 35$ min, $E_{las} \approx 60$ J cm^{-2}, and $P_{las} \approx 3 \times 10^9$ W cm^{-2}): (a) colloid with settled precipitate and (b) centrifuged colloid with precipitate.

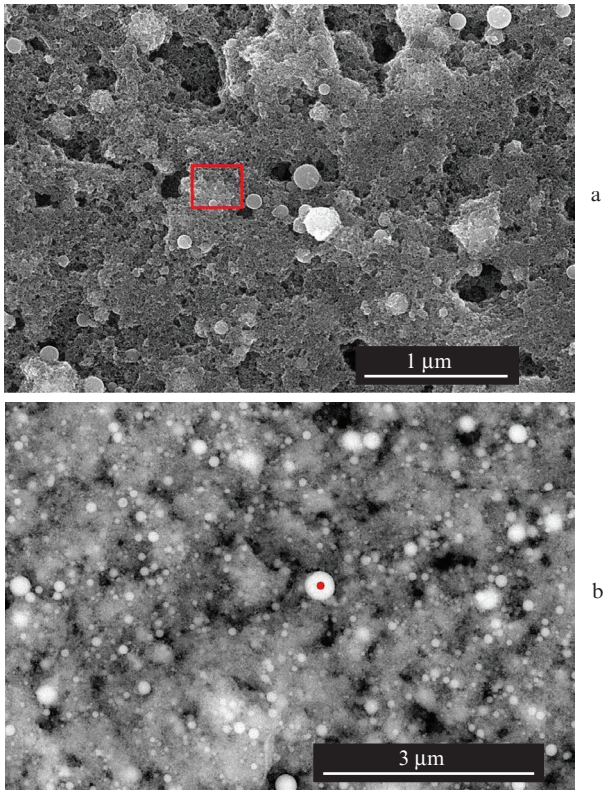

Figure 2. (Colour online) Morphology of dried precipitate from the transparent layer of colloid (Fig. 1a), obtained in the first irradiation regime: (a) secondary-electron and (b) backscattered-electron SEM images. The red lines and red dot indicate, respectively, the region boundaries and the point of EDS analysis.

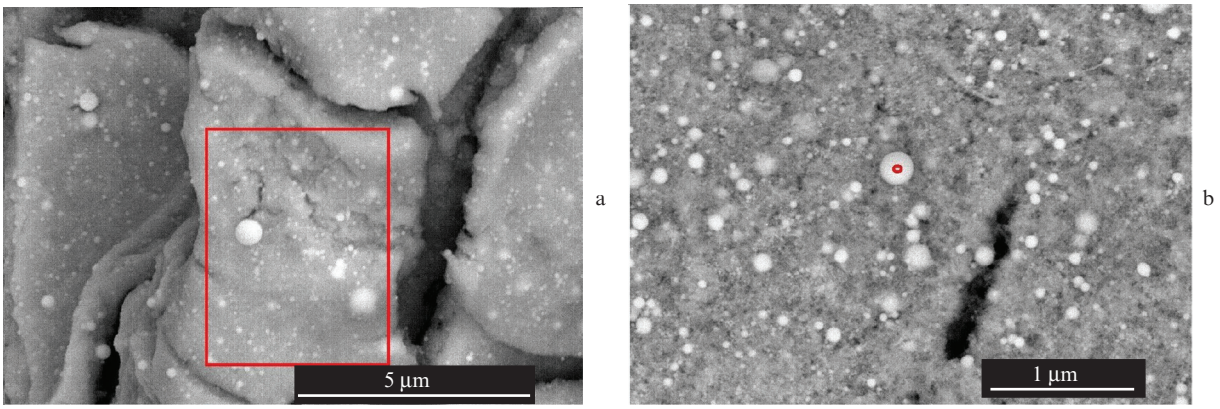

Figure 3. (Colour online) Morphology of dried precipitate from the carefully mixed colloid (Fig. 1a), obtained in the first irradiation regime: (a, b) backscattered-electron SEM images with different magnifications. The red lines and red dot indicate the region boundaries and the point of EDS analysis.

by selection and drying the transparent upper colloid layer (Fig. 1a) is presented in Fig. 2. It can be seen that the precipitate consists mainly of layers of agglomerates ~1–2 μm in size. These agglomerates are formed by (10–20)-nm nanoparticles. Bright spherical particles ~100–800 nm in size can be seen on the layer surface and in the bulk (Fig. 2b); many of them are covered by a fine-grained deposit.

Figure 3 shows SEM images of the precipitate obtained by drying the colloid shown in Fig. 1a, after its careful mixing. The pattern is essentially different. Large dense aggregates 5–10 μm in size were observed (Fig. 3a), with inclusions of bright spherical particles having sizes from several ten to several hundred nanometres, which can be seen well in the images. Since the outlines of the boundaries of large contacting aggregates practically coincide, we can suggest that these aggregates were formed as a result of cracking of unified solid mass (matrix of nanoparticles) during drying.

bottom residue was dried on substrates. The SEM images for this case are practically the same as the images presented in Fig. 3.

The morphology of the ablation products obtained in the second irradiation regime ($W \approx 1.0$ W, $\tau_{irr} \approx 50$ min, $E_{las} \approx 5$ J cm^{-2}, $P_{las} \approx 2.5 \times 10^8$ W cm^{-2}) is presented in Fig. 4. The colloid was dried directly after the target irradiation (prior to precipitation). The SEM study showed that the dried material formed in this regime is also based on a fractured matrix of nanoparticles (~10–20 nm in the cross section), saturated with nanospheres mainly ~50–600 nm in diameter.

In addition, newly formed aggregates can be observed in the matrix: fragments of hollow spheres (Fig. 4a) with walls several tens of nanometres thick and non-monotypic nanofibres with a thickness of ~30–100 nm and a length up to ~1 μm (Fig. 4b).

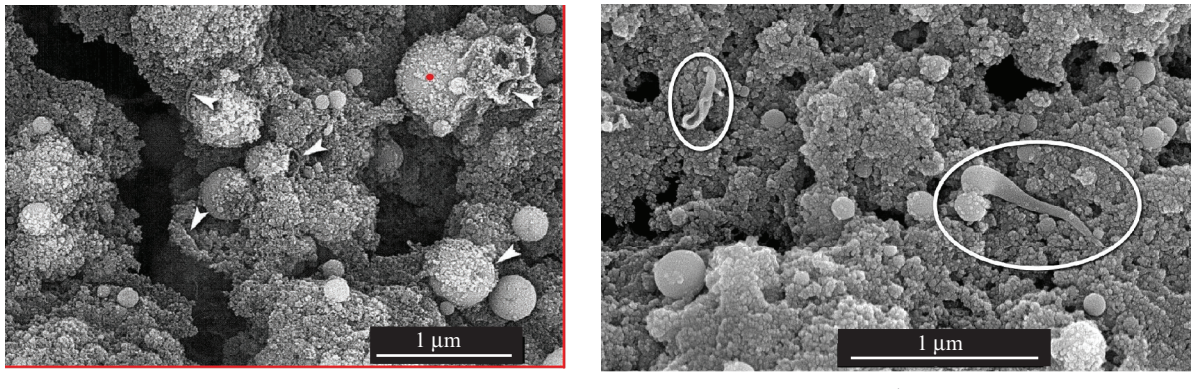

Figure 4. (Colour online) Morphology of the dried colloidal precipitate obtained in the second irradiation regime (backscattered-electron SEM image): (a) micro- and nanospheres and their fragments in the matrix of nanoparticles (the red dot indicates the point of EDS analysis) and (b) a fragment with nanofibres. Fragments and nanofibres are indicated by arrows and ellipses, respectively.

In regards to bright spherical nanoparticles, they have approximately the same characteristics as the similar particles in Fig. 2.

To study the morphology of the precipitate obtained by centrifugation of colloid (see Fig. 1b), the transparent part of the latter was poured out from the test tube, and the near-

3.2. Results of the EDS analysis of elemental composition

An EDS analysis was performed in the regions bordered by red lines in Figs 2a, 3a, and 4a. For the regions with transverse sizes significantly exceeding the diameter of the CXR generation region (~1.5 μm), the EDS data were averaged

over the region areas. Figure 5a shows as an example the elemental composition averaged over a region (Fig. 3a) of relatively large area (~20 μm^2) for the first irradiation regime. The elemental composition, averaged over an area of ~90 μm^2 (which is beyond the frames of Fig. 4a), for the second irradiation regime is presented in Fig. 5b. In both cases the main elements are titanium and oxygen; the O : Ti content ratio (in at%) in these regions is smaller than two and approximately the same. There is also a pronounced amount of Ca, Zn, Cu, Si, and C impurities (Fig. 5, inset). Small regions with cross sections smaller than the diameter of CXR generation region and the positioning points of immobile electron beam are shown in Figs 2a, 2b, 3b, and Fig. 4a. Note that a point analysis of the surface of observed microspheres is low-efficient in this case because the diameter of CXR generation region exceeds significantly their linear sizes; in addition, the spheres are coated to some extent by a layer of nanodispersed particles of the adjacent material. However, localisation of electron beam on spheres during the EDS analysis revealed a decrease in the content of impurities (Ca, Zn, Cu, Si, C) in comparison with that on small areas (Fig. 2a) in the material of the fractured matrix, which may indicate the absence of influence of these impurities on the formation of spheres.

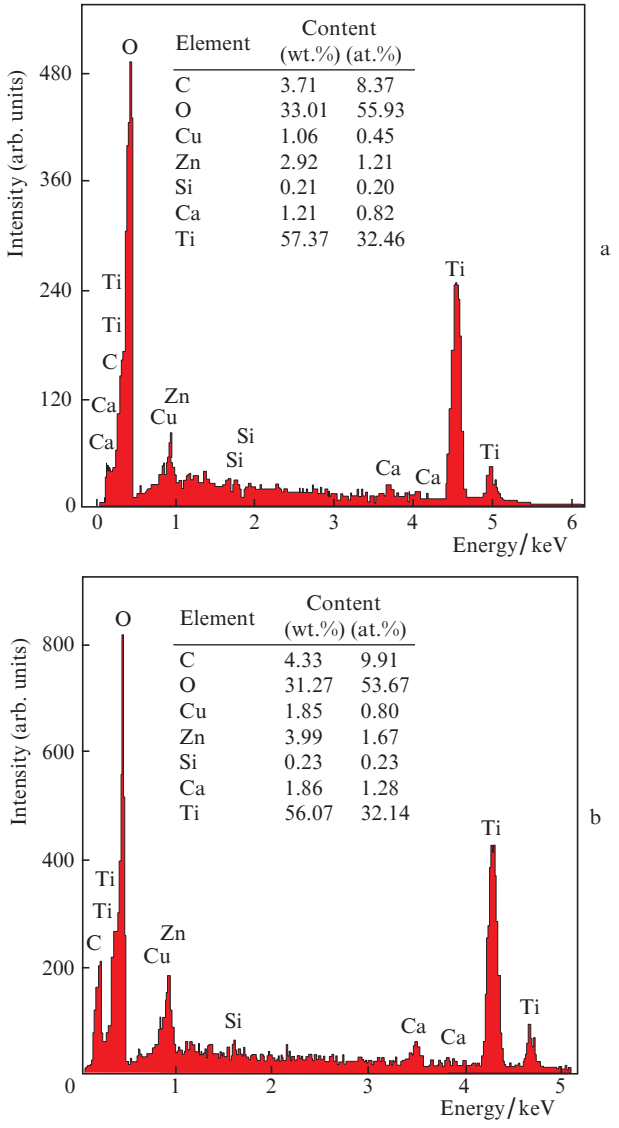

Figure 5. (Colour online) EDS data and elemental composition of the products of titanium ablation in water for the first irradiation regime (a) in the region with an area of ~20 μm^2, indicated by red lines in Fig. 3a, and (b) in the region with an area of ~90 μm^2, emerging beyond the fragment shown in Fig. 4a. The elemental contents in wt.% and at.% are given in the insets.

3.3. Results of the phase composition analysis

The X-ray diffraction spectrum of the precipitate obtained by drying the transparent upper layer of the colloid obtained in the first ablation regime (see Fig. 1a) does not contain any strong diffraction lines (Fig. 6a). One can see very weak maxima, which can be assigned to titanium oxides Ti_9O_{17} and TiO_2 and to titanium. Titanium dioxide is presented by two modifications: anatase and rutile. The size of coherent-scattering regions (CSRs) of the Ti_9O_{17} phase is 40 nm; the CSRs of the other phases are no less than 100 nm in size. The extended halo in the range of Bragg angles $2\theta = 16°–36°$ is due to the glass plate used as a substrate. The total content of the crystalline components having the aforementioned average CSR sizes in the precipitate is 1–2 vol%. These phases may also enter the precipitate composition in the X-ray amorphous state. On the whole, amorphous and, possibly, X-ray amorphous materials dominate in the product under consideration.

The X-ray diffraction spectrum of the precipitate obtained by drying the carefully mixed colloid (Fig. 1a) contains neither diffraction maxima nor diffuse halos (an exception is the substrate halo). This diffraction spectrum suggests that the precipitate under consideration is in amorphous and X-ray

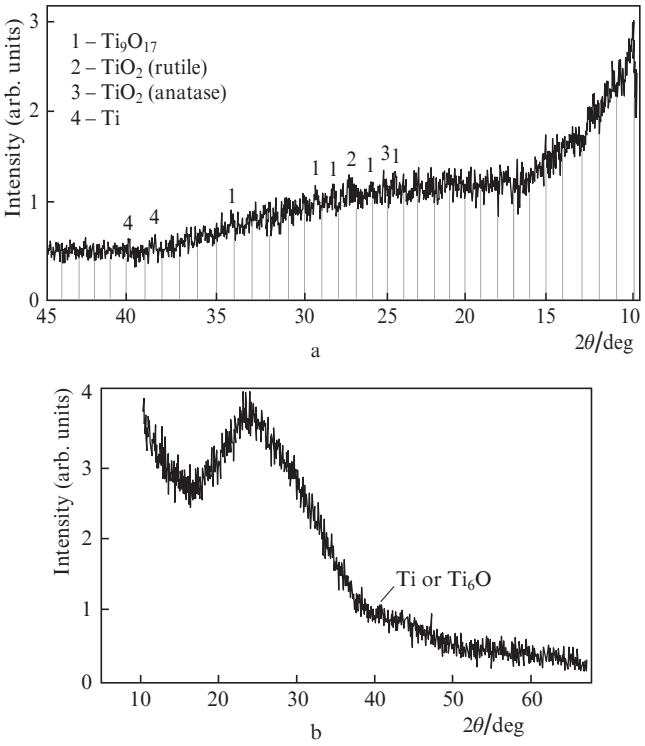

Figure 6. X-ray diffraction patterns of (a) the precipitate from dried upper transparent layer of the colloid obtained in the first ablation regime (Fig. 1a) (DRON-2 diffractometer) and (b) the precipitate obtained in the second ablation regime (SmartLab diffractometer); the weak halo in the range of angles $2\theta = 43°–49°$ is likely due to TiO.

amorphous states. It is likely that the contribution of the upper transparent layer (exhibiting the presence of well-crystallised phases) to the total precipitate mass is small, as a result of which the content of crystalline phases in the mixed colloid is below the XRD sensitivity limit.

The diffraction spectrum of the precipitate obtained by centrifugation of mixed colloid (Fig. 1b) contains a weak maximum corresponding to the interplanar spacing d = 0.205 nm. This maximum may belong to titanium oxide TiO with a hexagonal structure [15]. Along with the diffraction maximum, there is a weak diffuse halo in the range of Bragg angles $2\theta = 43°–49°$. One might expect this halo to be due to X-ray amorphous titanium oxide TiO. Note that the low intensity of the halo and the TiO line indicates dominance of the amorphous material in the test sample.

A halo similar to that described above is also observed in the X-ray diffraction spectrum (Fig. 6b) of the precipitate obtained in the second ablation regime (at low laser powers). It is likely that this halo belongs to titanium oxide TiO in the X-ray amorphous state. The weak diffraction maximum corresponding to the interplanar spacing d = 0.225 nm may be due to either metallic titanium or its oxide Ti_6O. The strong halo in the range of Bragg angles $2\theta = 16°–36°$ is due to the glass plate. The spectrum of the same test, recorded on a DRON-2 diffractometer with an X-ray beam of lower intensity, lacks a strong halo. On the whole, the X-ray diffraction spectrum shows the dominance of amorphous phase in the material under study.

The results of the qualitative analysis (using Raman spectroscopy) of a possible presence of crystallised nanoparticles in the ablation products under study are shown in Fig. 7. The known (see, e.g., [8, 16–18]) Raman spectra of pure anatase (peaks at frequencies of 143, 395, 516, and 635 cm^{-1}) and rutile (peaks at 144, 248, 443, and 614 cm^{-1}) with crystallites ~1 μm in size are shown for comparison in the upper part of Fig. 7. The Raman spectra of the precipitates of colloids obtained in two irradiation regimes are presented in the lower part. The spectrum of the dried precipitate shown in Fig. 3, obtained in the first irradiation regime [Fig. 7, curve (*1*)], exhibits a strong anatase line (near the peak at 143 cm^{-1}) and a broadened rutile line (in the vicinity of 443 and 614 cm^{-1}). Highly diffuse weak lines of rutile and a very weak anatase line are observed for the precipitate obtained in the second irradiation regime at a lower laser power [curve (*2*)]. No other Raman lines (in particular, the line of TiO crystallites, whose possible presence in small amounts was evidenced by XRD data) were observed for the samples produced in both irradiation regimes. Note that, according to [19], Raman spectra are insensitive to TiO.

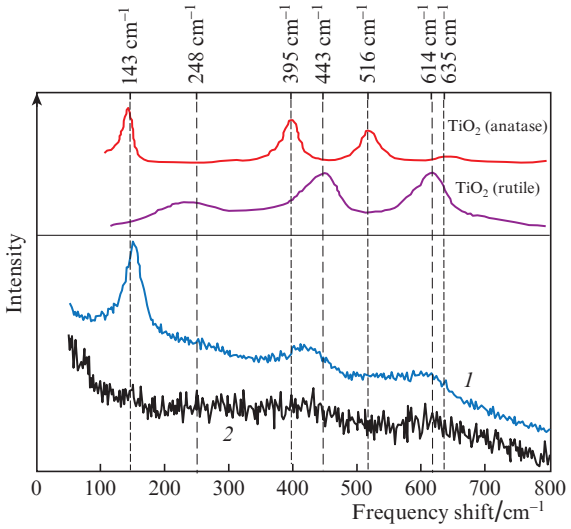

Figure 7. (Colour online) Raman spectra of the products of titanium ablation in water: the precipitate (see Fig. 3) obtained in the first (*1*) and second (*2*) target irradiation regimes. The Raman spectra of pure rutile and anatase are shown in the top.

In the vicinity of the peak at a frequency of 143 cm^{-1} in curve (*1*), the FWHM of the first strong Raman line of anatase was ~35 cm^{-1}. Judging from the data in the literature [16], this linewidth may correspond to anatase crystallite sizes of 3–4 nm. This fact is in favour of the proximity of anatase (and, possibly, other titanium oxides) to the X-ray amorphous state.

4. Discussion of the results

Summing up the XRD and Raman spectroscopy data, we can conclude that the volume fraction of crystallised titanium oxides in all dried precipitates formed in both irradiation regimes is very small. At the same time, crystallites of different oxides (including TiO) can be identified in the precipitates obtained in the first regime. The TiO compound produced in the second irradiation regime exists apparently only in the X-ray amorphous state.

Let us compare our results with the data of some other studies. For example, nanoparticles of nonstoichiometric oxide $TiO_{1.04}$ ~35 nm in size were obtained in [7] as a result of titanium ablation in water under irradiation by a CVL, whose parameters are close to the second-regime parameters ($E_{las} \approx 4$ J cm^{-2}, $P_{las} \approx 2 \times 10^8$ W cm^{-2}, and f = 15 kHz). Strong clear peaks could be observed in the corresponding diffraction patterns. The volume fraction of crystallites and target irradiation time were not indicated in that study. Guilléna et al. [4], who used Nd:YAG laser pulses with close parameters (λ = 0.532 μm, $\tau_p \approx 10$ ns, E_{las} = 2.8–27.6 J cm^{-2}, $P_{las} \approx 2.8 \times 10^8$–$2.76 \times 10^9$ W cm^{-2}) but much lower pulse repetition rate and shorter irradiation time (f = 10 Hz, τ_{irr} = 5 min), obtained a dried product of titanium ablation in water, which consisted mainly of spherical crystallites 12–15 nm in diameter and their agglomerates. The ablation products contained crystallised rutile and anatase nanoparticles of the same composition as in our study and, additionally, Ti_8O_{15}. With τ_{irr} increased to 30 min in [20] (at λ = 0.532 μm, $\tau_p \approx 5$ ns, $E_{las} \approx 1$ J cm^{-2}, $P_{las} \approx 2 \times 10^8$ W cm^{-2}), more than 85% nanoparticles had a size less than 5 nm, whereas at large E_{las} (~10 J cm^{-2}) and P_{las} ($\sim 2 \times 10^9$ W cm^{-2}) values the nanoparticle sizes did not change significantly, but (100–200)-nm agglomerates, consisting of these nanoparticles, arose.

It was shown in [8] (for λ = 1.062 μm, f = 10 Hz, τ_{irr} = 5 min) that, at small P_{las} values (of no more than 1×10^8 W cm^{-2}), titanium ablation in water leads to the formation of mainly TiO, Ti_2O_3, and TiO_2 crystallites. The amorphous phase fraction was small. At very large P_{las} values ($\sim 1 \times 10^{11}$ W cm^{-2}) amorphous phase dominated in the ablation products, and TiO_2 crystallites were mainly present. It was suggested that the phase amorphisation may occur via dynamic condensation and a very fast process of particle cooling in water, as well as due to the shock-wave loading upon formation of a bubble (retained by the liquid) on the target surface. It is possible that these processes occurred also

to some extent under our experimental conditions (with a CVL). The P_{las} value exceeded some critical power necessary for implementing the ablation regime of target irradiation. In addition, the high pulse repetition rate (10 kHz) and long irradiation time (30–50 min) could facilitate the production of very small (~2 nm in size) nanoparticles, i.e., the occurrence of a significant fraction of X-ray amorphous phase. Indeed, the production of particles should become more efficient with an increase in the radiation energy absorbed by the target and the particles falling in the beam waist region during irradiation. This energy is proportional to the total laser energy, $E_f = E_p f \tau_{irr}$, introduced into the liquid for the irradiation time. In [4], where the degree of crystallinity of the ablation products was high, the E_f value was as small as ~700 J. Dominance of the amorphous fraction over crystalline in the ablation products at $E_f \approx 1.8 \times 10^3$ J was observed in [8]. In our study, we had $E_f \approx 2.7 \times 10^4$ in the first irradiation regime and $E_f \approx 5.4 \times 10^3$ J in the second regime; both these values exceed significantly the corresponding energy values in the aforementioned studies. This is a possible explanation of the fact that the ablation products obtained by us were mainly in the amorphous (or X-ray amorphous) state.

In our previous works [21, 22] we investigated the ablation of some transition metals (Cu, Zn, Zr, W, Mo, V) in liquids using a CVL in the first irradiation regime. It was found that the morphologies of the products of ablation in water for all considered metals, as well as for titanium, are similar both in the set of structural forms and in the type of agglomeration of these forms. Most of the material was also in the amorphous state; the rest were crystalline phases of metal oxides.

5. Conclusions

The results of studying the titanium ablation in distilled water using a repetitively pulsed CVL in a wide range of power and energy densities at a pulse repetition rate of 10 kHz and irradiation time of 30–50 min are presented. Insignificant differences were revealed in the morphologies of nanostructures of dried precipitates formed in ablation regimes with high and low irradiation powers. It is shown that the volume fraction of crystalline phases if all synthesised titanium oxides is small: no more than ~1%–2%. Most of the ablation products obtained in all irradiation regimes are in the X-ray amorphous and amorphous states. These nanoproducts from different titanium oxides may be of great practical interest for various applications.

Acknowledgements. We are grateful to N.N. Mel'nik for recording and analysing Raman spectra and to V.Ya. Pecherkin and O.V. Sazhnova for the help in carrying out experiments.

References

1. Simakin A.V., Voronov V.V., Shafeev G.A. *Trudy IOFAN*, **60**, 83 (2004).
2. Yang G.W. *Prog. Mater. Sci.*, **52** (4), 648 (2007).
3. Shafeev G.A., in *Lasers in Chemistry. V. 2. Influencing Matter* (Wienheim: Wiley-VCH, 2008) pp 713–741.
4. Guilléna G.G., Shaji S., Palma M.I.M., Avellaneda D.A., Castillo G.A., Roy T.K.D., Gutiérrez D.I.G., Krishnan B. *Appl. Surf. Sci.*, **405**, 183 (2017).
5. DongShi Zhang, Jun Liu, ChangHao Liang. *Sci. China-Phys. Mech. Astron.*, **60**, 074201 (2017).
6. Borodina T.I., Val'yano G.E., Gololobova O.A., Karpukhin V.T., Malikov M.M., Strikanov D.A. *Quantum Electron.*, **43** (6), 563 (2013) [*Kvantovaya Elektron.*, **43** (6), 563 (2013)].
7. Dolgaev S.I., Simakin A.V., Voronov V.V., et al. *Appl. Surf. Sci.*, **186**, 546 (2002).
8. Huang C.-N., Bow J.-S., Zheng Y., Chen S.-Y., Jin Ho N., Shen P. *Nanoscale Res. Lett.*, **5**, 972 (2010).
9. Chen X., Mao S.S. *Chem. Rev.*, **107**, 2891 (2007).
10. Park H., Park Y., Kim W., Choi W. *J. Photochem. Photobiol. C: Photochem. Rev.*, **15**, 1 (2013).
11. Gurbatov S.O., Mincheva N., Ivamori S., Kulinich S.A., Kuchmizhak A.A. *Quantum Electron.*, **50** (9), 855 (2020) [*Kvantovaya Elektron.*, **50** (9), 855 (2020)].
12. Varaksin A.Yu. *Dokl. Phys.*, **66**, 72 (2021) [*Dokl. Ross. Akad. Nauk., Ser. Fiz.Tekh. Nauki*, **497**, 36 (2021)].
13. Varaksin A.Yu. *High Temperature*, **58** (5), 716 (2020).
14. Karpukhin V.T., Kazaryan M.A., Protasov M.V., Malikov M.M., Borodina T.I., Val'yano G.E., Gololobova O.A. *Kratk. Soobshch. Fiz. FIAN*, (6), 22 (2017) [*Bull. Lebedev Phys. Inst.*, **44** (6), 168 (2017)].
15. Moehr S., Mueller-Buschbaum H., Anorg Z. *Allg. Chem.*, **620**, 1175 (1994).
16. Swamy V., Kuznetsov A., Dubrovinsky L.S., Caruso R.A., Shchukin D.G., Muddle B.C. *Phys. Rev. B*, **71**, 1 (2005).
17. Zuñiga-Ibarra V.A., Shaji S., Krishnan B., Johny J., Kanakkillam S.S., Avellaneda D.A., Martinez J.A.A., Roy T.K.D., Ramos-Delgado N.A. *Appl. Surf. Sci.*, **483**, 156 (2019).
18. Xiao W.S., Hong Z., Tan D.Y., Weng K.N., Li Y.C., Luo C.J., Jing L., Xie H.S. *Spectrosc. Spectral Anal.*, **27**, 1340 (2007).
19. Del Pino A.P., Serra P.S., Morenza J.L. *Surf. Coat. Technol.*, **187**, 106 (2004).
20. Barreca F., Acacia N., Barletta E., Spadaro D., Currт G., Neri F. *Appl. Surf. Sci.*, **256**, 6408 (2010).
21. Borodina T.I., Val'yano G.E., Karpukhin V.T., Malikov M.M., Kazaryan M.A. *Kratk. Soobshch. Fiz. FIAN*, (7), 3 (2020) [*Bull. Lebedev Phys. Inst.*, **47** (7), 191 (2020)].
22. Malikov M.M., Val'yano G.E., Borodina T.I. *Quantum Electron.*, **51** (6), 544 (2021) [*Kvantovaya Elektron.*, **51** (6), 544 (2021)].